

The MOSDEF Survey: The First Direct Measurements of the Nebular Dust Attenuation Curve at High Redshift*

Naveen A. Reddy¹ , Alice E. Shapley² , Mariska Kriek³ , Charles C. Steidel⁴ , Irene Shivaei⁵,¹¹ , Ryan L. Sanders⁶,¹¹ , Bahram Mobasher¹, Alison L. Coil¹ , Brian Siana¹ , William R. Freeman¹ , Mojegan Azadi³ , Tara Fetherolf¹ , Gene Leung¹ , Sedona H. Price⁵ , and Tom Zick³¹ Department of Physics and Astronomy, University of California, Riverside, 900 University Avenue, Riverside, CA 92521, USA; naveenr@ucr.edu² Department of Physics & Astronomy, University of California, Los Angeles, 430 Portola Plaza, Los Angeles, CA 90095, USA³ Astronomy Department, University of California, Berkeley, Berkeley, CA 94720, USA⁴ Cahill Center for Astronomy and Astrophysics, California Institute of Technology, MC 249-17, Pasadena, CA 91125, USA⁵ Steward Observatory, University of Arizona, 933 North Cherry Avenue, Tucson, AZ 85721, USA⁵ Department of Physics, University of California, Davis, One Shields Avenue, Davis, CA 95616, USA⁴ Center for Astrophysics and Space Sciences, University of California, San Diego, 9500 Gilman Drive, La Jolla, CA 92093-0424, USA⁶ Harvard-Smithsonian Center for Astrophysics, 60 Garden Street, Cambridge, MA 02138, USA⁶ Max-Planck-Institut für Extraterrestrische Physik, Postfach 1312, Garching, D-85741, Germany Received 2020 July 4; revised 2020 August 27; accepted 2020 September 7; published 2020 October 20

Abstract

We use a sample of 532 star-forming galaxies at redshifts $z \simeq 1.4$ –2.6 with deep rest-frame optical spectra from the MOSFIRE Deep Evolution Field (MOSDEF) survey to place the first constraints on the nebular attenuation curve at high redshift. Based on the first five low-order Balmer emission lines detected in the composite spectra of these galaxies (H α through H ϵ), we derive a nebular attenuation curve that is similar in shape to that of the Galactic extinction curve, suggesting that the dust covering fraction and absorption/scattering properties along the lines of sight to massive stars at high redshift are similar to those of the average Milky Way sight line. The curve derived here implies nebular reddening values that are, on average, systematically larger than those derived for the stellar continuum. In the context of stellar population synthesis models that include the effects of stellar multiplicity, the difference in reddening of the nebular lines and stellar continuum may imply molecular cloud crossing timescales that are a factor of $\gtrsim 3 \times$ longer than those inferred for local molecular clouds, star formation rates that are constant or increasing with time such that newly formed and dustier OB associations always dominate the ionizing flux, and/or that the dust responsible for reddening the nebular emission may be associated with nonmolecular (i.e., ionized and neutral) phases of the interstellar medium. Our analysis points to a variety of investigations of the nebular attenuation curve that will be enabled with the next generation of ground- and space-based facilities.

Unified Astronomy Thesaurus concepts: Interstellar dust extinction (837); Galaxy evolution (594); High-redshift galaxies (734); Interstellar dust (836); Interstellar reddening (853); Interstellar extinction (841); Reddening law (1377)

1. Introduction

Recent advances in near-infrared detector technology and multiplexing capabilities have led to a rapid increase in the number of rest-frame optical ($\lambda \simeq 3700\text{-}6700~\text{Å}$) line measurements for high-redshift ($1.4 \lesssim z \lesssim 3.8$) galaxies, numbering now in the thousands (e.g., Förster Schreiber et al. 2009; Kashino et al. 2013; Steidel et al. 2014; Kriek et al. 2015). In turn, these measurements have yielded valuable insights into the dust reddening, gas-phase metallicities, star formation rates (SFRs), and physical state of the gas in the interstellar medium (ISM) of high-redshift galaxies. Critical to many of these inferences is the wavelength dependence of dust obscuration of the ionized gas (i.e., the nebular dust attenuation curve), typically assumed to follow that of the average Milky Way (MW) sight line (Cardelli et al. 1989).

The customary approach to deducing the attenuation of the nebular emission and stellar continuum in galaxies is to assume that each is subject to a different attenuation curve (even if the intrinsic dust extinction curve is the same throughout the galaxy), stemming from the expectation that the young stars that dominate the nebular emission are located preferentially in regions with higher dust covering fractions associated with their parent molecular clouds (e.g., with a geometry approximating a foreground screen of dust; Calzetti et al. 1994). In particular, for nearby starburst galaxies, the Galactic extinction curve (Cardelli et al. 1989) is commonly adopted for the nebular line emission, whereas an attenuation curve (i.e., one that accounts for the scattering of light into the line of sight and for a nonuniform distribution of column densities; e.g., Calzetti et al. 2000) is assumed for the stellar continuum (e.g., Calzetti et al. 1994; Calzetti 1997). Separately, a number of studies of both local (Fanelli et al. 1988; Calzetti 1997; Calzetti et al. 2000; Wild et al. 2011; Kreckel et al. 2013) and high-redshift star-forming galaxies (e.g., Förster Schreiber et al. 2009; Yoshikawa et al. 2010; Wuyts 2011; Kashino et al. 2013; Wuyts 2013; Price et al. 2014; Reddy et al. 2015; De Barros et al. 2016; Buat et al. 2018; Shivaei et al. 2020) have found that the line emission arising from the nebular (ionized gas) regions is subject to a higher degree of reddening than the nonionizing stellar continuum emission, perhaps reflecting a variation in the column density of dust as viewed along the average sight lines to differently aged stellar populations within

^{*} Based on data obtained at the W.M. Keck Observatory, which is operated as a scientific partnership among the California Institute of Technology, the University of California, and NASA and was made possible by the generous financial support of the W.M. Keck Foundation.

¹⁰ NASA Hubble Fellow.

galaxies. Together, the variations in the shape of the attenuation curve and column density of dust point to a complicated geometry of dust and stars that varies significantly from galaxy to galaxy.

There has been much debate regarding the appropriate curve to use for the stellar continuum in high-redshift galaxies. However, the shape of the nebular attenuation curve—and whether it is similar to that of the stellar continuum—has received little attention despite its importance in deducing several key physical attributes of the ISM, such as gas-phase metallicity and ionization state. Given that the nebular attenuation curve underpins many of the most fundamental properties that we can infer for the ISM in galaxies, and that there is no a priori reason why the curve should follow that of the average MW sight line (e.g., due to potential differences in grain composition and/or distribution, structure of molecular clouds, etc.), it is imperative to directly probe the shape and normalization of this curve at high redshift. From a practical standpoint, the derivation of the nebular attenuation curve is simpler than that of the stellar attenuation curve; the former can be accomplished using recombination emission lines whose strengths are dictated by well-understood physics, while the latter typically relies on uncertain assumptions for the intrinsic stellar spectrum of a galaxy. At any rate, comparison of the nebular and stellar attenuation curves provides important insights into the spatial distribution and properties of the dust for differently aged stellar populations in galaxies.

Only with the recent accumulation of a large number of spectroscopic measurements of recombination emission lines in high-redshift galaxies has it been possible to directly constrain both the shape and normalization of the nebular dust attenuation curve. Here we use extensive spectroscopy of the Balmer recombination emission lines of high-redshift ($z \simeq 1.4$ –2.6) star-forming galaxies in the MOSFIRE Deep Evolution Field (MOSDEF; Kriek et al. 2015) survey to place the first direct constraints on the nebular attenuation curve at high redshift.

The translation between a single Balmer emission line ratio (e.g., $H\alpha/H\beta$) and the nebular reddening, $E(B-V)_{\rm neb}$, depends on the shape of the extinction/attenuation curve. Consequently, a single line ratio cannot be used to uniquely identify the shape of the dust curve. However, with multiple Balmer emission line ratios constructed with at least three Balmer recombination lines, we can simultaneously constrain both the reddening and the shape of the dust curve. The deep near-IR spectroscopy of the MOSDEF survey covers different subsets of the Balmer recombination emission lines, depending on the redshift of each galaxy. For this study, we have focused on the first five low-order Balmer emission lines, listed in Table 1, that are significantly detected in either individual galaxy spectra ($H\alpha$, $H\beta$, and occasionally $H\gamma$ and $H\delta$) or composite spectra of ensembles of galaxies.

The outline of this paper is as follows. Section 2 describes the parent MOSDEF sample and some of the steps in the spectroscopic data reduction that are salient to the determination of the nebular attenuation curve. We also describe the method used for constructing composite spectra and measuring line ratios from these composites. Section 3 focuses on the various subsamples used to construct composites, while the calculation of the shape of the nebular attenuation curve is presented in Section 4. In Section 5, we compare the nebular attenuation curve with other common extinction/attenuation

Table 1
Balmer Recombination Lines

Line	$\lambda \ (\mathring{A})^a$	I ^b	Fitting Window (Å) ^c
$H\alpha^{\mathbf{d}}$	6564.60	2.860	6482–6652
$H\beta$	4862.71	1.000	4813-4913
$H\gamma$	4341.69	0.468	4301-4383
$H\delta$	4102.89	0.259	4055-4160
$H\epsilon^{e}$	3971.20	0.159	3946-4024

Notes.

curves. In Section 6, we present a comparison of nebular and stellar reddening and discuss differences in these two quantities in the context of stellar population models that include the effects of stellar multiplicity. Wavelengths are presented in the vacuum frame. We adopt a cosmology with $H_0 = 70 \, \mathrm{km \, s^{-1} \, Mpc^{-1}}$, $\Omega_{\Lambda} = 0.7$, and $\Omega_{\mathrm{m}} = 0.3$.

2. Survey and Basic Measurements

2.1. MOSDEF Survey

The MOSDEF survey (Kriek et al. 2015) used the MOSFIRE instrument (McLean et al. 2012) on the Keck telescope to acquire moderate-resolution ($R \sim 3000-3600$) rest-frame optical spectra of ≈ 1500 H-band selected galaxies at redshifts $1.4 \lesssim z \lesssim 3.8$ in the CANDELS fields (Grogin et al. 2011; Koekemoer et al. 2011). Galaxies were targeted for spectroscopy based on preexisting spectroscopic, grism, or photometric redshifts that placed them in three redshift ranges -z = 1.37-1.70, 2.09-2.70, and 2.95-3.80—where the strong rest-frame optical emission lines lie in the YJH, JHK, and HK transmission windows, respectively. Spectral data were reduced and extracted as described in Kriek et al. (2015).

2.2. Slit Loss Corrections

The method employed here to determine the nebular attenuation curve relies on taking ratios of multiple Balmer emission lines. In general, these lines fall in multiple near-IR filters that were observed in different weather and seeing conditions. Reliable determinations of the line ratios thus require accurate relative flux calibration of the spectra taken in different filters. To this end, bright "slit stars" were observed simultaneously with the target galaxies in order to flux calibrate the spectra and compute first-order corrections for slit losses. Because the galaxies are spatially resolved given their typical sizes and the seeing of the observations, second-order corrections for slit losses—based on modeling the light profiles of the galaxies—were applied to the spectra (Kriek et al. 2015; Reddy et al. 2015). The efficacy of our slit loss correction procedure was evaluated by comparing the spectroscopic flux densities of galaxies detected in the continuum with their

^a Rest-frame vacuum wavelength, taken from the Atomic Spectra Database of the National Institute of Standards and Technology (NIST), https://www.nist.gov/pml/atomic-spectra-database.

Intensity of line relative to H β for Case B recombination, $T_e = 10$, 000 K, and $n_e = 100 \text{ cm}^{-3}$.

^c Wavelength window over which line fitting was performed.

^d The H α was fit simultaneously with the [N II] doublet (Section 2.6).

^e The H ϵ is blended with [Ne III] $\lambda 3969$. The contribution of the latter was estimated by measuring [Ne III] $\lambda 3870$ (Section 3), for which we assumed a rest-frame vacuum wavelength of 3869.86 Å and a fitting window that spans the range $\lambda = 3851$ –3882 Å.

broadband flux densities. This comparison shows that the slit loss-corrected spectra yield flux densities that are typically within $\simeq 18\%$ of the broadband values (e.g., Reddy et al. 2015). Moreover, averaging the slit loss-corrected spectra for individual galaxies results in composite spectra whose shapes agree with those of the average broadband spectral energy distributions (SEDs) of the same galaxies (Section 2.5).

2.3. Line Flux Measurements

Line fluxes for individual objects were measured from the spectra by fitting Gaussian functions on top of a linear continuum. Two Gaussian functions were used to fit the [O II] doublet, while three were used to simultaneously fit $H\alpha$ and the [N II] doublet. Gaussian functions were assumed for all other lines. As the continuum is generally not detected in the spectra of individual galaxies, the fluxes of Balmer emission lines were also calculated assuming an underlying linear continuum. As such, the Balmer emission line measurements for individual galaxies are not corrected for underlying Balmer absorption. However, as we discuss below, Balmer absorption is taken into account when measuring average line fluxes in the composite spectra of galaxies. Errors in line fluxes were derived by allowing the spectra to vary 500 times according to the error spectra and remeasuring the line fluxes from these realizations. For this study, active galactic nuclei (AGNs) were excluded based on the IR, X-ray, and rest-frame optical line flux criteria as described in Coil et al. (2015), Azadi et al. (2017, 2018), and Leung et al. (2019). Further details on target selection, observations, spectroscopic data reduction, slit loss corrections, and line flux measurements are provided in several papers discussing results from the MOSDEF survey (e.g., Kriek et al. 2015; Reddy et al. 2015).

2.4. Stellar Population Modeling

To aid in fitting the Balmer emission lines while accounting for underlying Balmer absorption, we computed the stellar population models that best fit the photometry of galaxies in our sample. We fit the Bruzual & Charlot (2003, hereafter BC03) Z = 0.020 "solar"-metallicity stellar population synthesis models to broadband photometry compiled in Skelton et al. (2014). If applicable, the photometry was corrected for the contribution from the strongest rest-frame optical emission lines measured in the MOSFIRE spectra, including [O II], H β , [O III], H α , and [N II]. We assumed a constant star formation history and ages that vary from 50 Myr to the age of the universe at the redshift of each galaxy. We considered stellar continuum reddening in the range $0.0 \le E(B-V)_{\text{stars}} \le 0.6$ for the Reddy et al. (2015) curve, which was derived from MOSDEF galaxies targeted during the first 2 yr of the survey. In Section 6, we also consider other stellar attenuation curves that may be more applicable to galaxies in the lower and upper halves of the stellar mass distribution of MOSDEF galaxies. The stellar mass, age, $E(B-V)_{\text{stars}}$ (i.e., reddening of the stellar continuum), and SFR of the model that yields the lowest χ^2 relative to the photometry were taken to be the "best-fit" values, and the bestfit models themselves were used in fitting the Balmer emission lines (Section 2.6).

2.5. Composite Spectra

The weaker Balmer lines, e.g., $H\gamma$ and the higher-order transitions, are typically not detected in the spectra of individual objects. In order to obtain robust constraints on the shape of the nebular attenuation curve at wavelengths shorter than $H\gamma$, we constructed composite spectra that allow us to detect these weaker Balmer lines. The procedure for constructing these composite spectra proceeded as follows.

First, the science and error spectra were shifted to the rest frame, converted to luminosity density, and interpolated to a grid with a wavelength spacing of $\delta \lambda_{\rm g} = 0.5 \, \text{Å}$. Error spectra were multiplied by $\sqrt{\delta \lambda_n/\delta \lambda_g}$ to account for resampling, where $\delta \lambda_n$ is the native wavelength spacing of the spectra. The science and error spectra were then normalized by the H α luminosity measured from the science spectrum. The composite spectrum at each wavelength point was computed as an unweighted average with 3σ outlier rejection of the luminosity densities of individual spectra at the same wavelength point. The composite error spectrum was calculated by adding in quadrature individual error spectra and dividing by the total number of individual spectra contributing to a given wavelength point. Figure 1 shows an example of one of the composite spectra, along with the fits to the Balmer lines (see Section 2.6). The average best-fit SED corresponding to a composite spectrum was computed by simply averaging the best-fit SEDs of individual galaxies contributing to that composite spectrum. This average best-fit SED aids in measuring the Balmer lines, as discussed in the next section.

2.6. Balmer Line Ratio Measurements from the Composite Spectra

Average Balmer emission line ratios were computed from the composite spectra as follows. Each Balmer emission line was fit with one Gaussian function (see below for exceptions) on top of a continuum with a shape given by the average bestfit SED for that composite. By fixing the shape of the underlying continuum to that of the average best-fit SED, we can account for underlying Balmer absorption and, in the case of H ϵ , additional absorption from the Ca II H line. The Balmer absorption line profiles in the average best-fit SEDs generally agree well with the absorption line profiles observed in the corresponding composite spectra (Figure 1). The velocity widths of the Gaussian functions used to fit the Balmer emission lines were fixed to lie within 20% of the value obtained for $H\alpha$. We also allowed the centers of the Gaussian functions to vary within 1.5 Å of the rest-frame values listed in Table 1. The H α line was fit simultaneously with the [N II] doublet using three Gaussian functions.¹

Additionally, H ϵ is blended with the longer-wavelength line of the [Ne III] $\lambda\lambda 3870$, 3969 doublet. The H ϵ + [Ne III] $\lambda 3969$ blend is marginally resolved in our spectra (Figure 1). Thus, the H ϵ flux was calculated by simultaneously fitting both the H ϵ and [Ne III] $\lambda 3969$ lines with two Gaussian functions, where the flux of [Ne III] $\lambda 3969$ was fixed to be $\approx 31\%$ of the flux of [Ne III] $\lambda 3870$, and the velocity width of [Ne III] $\lambda 3969$ was fixed to that of [Ne III] $\lambda 3870$.

 $[\]overline{^{11}}$ The composite $H\alpha$ line profile is slightly broadened relative to a Gaussian function. Given the lack of a broadened component in the $H\beta$, [O II], and [O III] lines, we chose to fit a single Gaussian to the $H\alpha$ line. Separately fitting the broadened component of this line results in a total $H\alpha$ luminosity that is $\simeq 1\%$ larger than that obtained with a single Gaussian function.

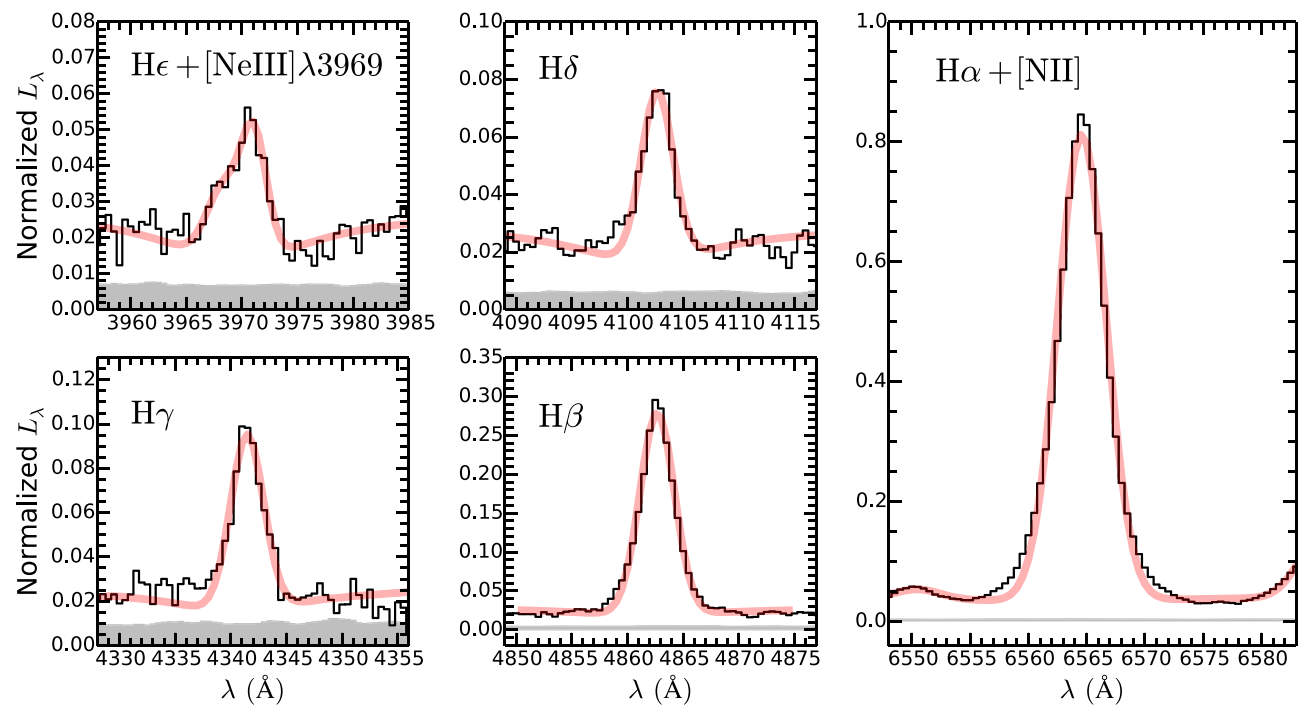


Figure 1. Composite spectrum constructed for sample S4 (Table 2), shown in black, along with fits to each of the Balmer emission lines (red). The error spectrum is indicated in gray. For sample S4, only H α , H β , and H ϵ were used to compute the attenuation curve (Section 3).

We considered only the first five low-order Balmer emission lines in our analysis. We did not use $H\zeta$ to calculate the dust curve, as this line is blended (and unresolved) with the He I $\lambda 3889$ triplet line. Moreover, the higher-order recombination lines are not only intrinsically weaker than the lower-order lines, but, if dust is present, they are progressively attenuated given their shorter wavelengths. In our analysis, $H\eta$, $H\theta$, $H\iota$, and all other higher-order Balmer emission lines, as well as the higher-order Paschen lines that have coverage in the MOSFIRE spectra (e.g., $P\delta$ and higher for galaxies at $z\sim 1.4$, $P\iota$ and higher at $z\sim 2.0$, and so on), were not considered, as none of these lines are detected with a signal-to-noise ratio $(S/N)\geqslant 3$ in any of the composite spectra considered here.

Each Balmer emission line was fit by considering only those wavelength points lying in the windows specified in Table 1 and allowing the continuum normalization to vary. Because the individual galaxy spectra were normalized by the $H\alpha$ fluxes before combining them into composites (Section 2.5), the line measurements obtained from these composites represent the average ratios of the line luminosities to that of $H\alpha$. All of the fitting described above, along with the line flux error calculations, was implemented using IDL's MPFIT package (Markwardt 2009).

3. Sample Construction for Nebular Attenuation Curve Analysis

The most robust and useful constraints on the shape of the nebular dust attenuation curve can be obtained from large samples of galaxies with coverage of as many H I (or other) recombination emission lines as possible. Large samples allow us to measure the average emission line fluxes with greater precision and detect weaker recombination lines, while coverage of many lines allows us to determine the shape of the dust curve over a broad range of wavelengths.

The method of using multiple recombination line ratios to constrain the shape of the nebular dust attenuation curve relies on the assumption that the optical depths (τ) of all of the line transitions are less than a few. In particular, for very dusty galaxies, the variation in optical depth with wavelength could result in a situation where the high-order Balmer recombination lines are dominated by emission from the relatively unobscured regions of a galaxy, while the low-order lines are dominated by emission from the dustier and potentially physically distinct regions of a galaxy. In this scenario, one would deduce less attenuation at bluer wavelengths. The average $E(B-V)_{neb}$ of galaxies in our sample, derived assuming the Galactic (MW) extinction curve (Cardelli 1989), $\langle E(B-V)_{\rm neb}\rangle \simeq 0.35$, with $\gtrsim 90\%$ of the galaxies having $E(B-V)_{\text{neb}} < 0.7$. Based on this $E(B-V)_{\text{neb}}$ distribution, we expect $\tau(H\epsilon) \lesssim 2$ for typical galaxies in our sample, with the vast majority having $\tau(H\epsilon) \lesssim 4$ (Figure 2), suggesting that the wavelength variation in optical depth is unlikely to affect our determination of the nebular dust attenuation curve.¹

Nevertheless, when using the ratios of these recombination lines to compute the shape of the dust curve, we must take care that the distribution of nebular reddening of individual galaxies contributing to each line is identical. Simply put, we must ensure that exactly the same set of galaxies contributes to each of the lines. As the galaxies in our sample span a range of redshifts and may have been observed in different sets of filters, not all galaxies that have coverage of one emission line will have coverage in others.

To ensure that the same set of galaxies contributes to each line used to compute the nebular attenuation curve, we subdivided our sample into sets of galaxies that have various combinations of covered emission lines in common. We

 $[\]overline{^{12}}$ The attenuation curve determined from only those galaxies that have $E(B-V)_{\rm neb} < 1$, as calculated with the MW curve, is identical within the errors to the one found using the entire sample.

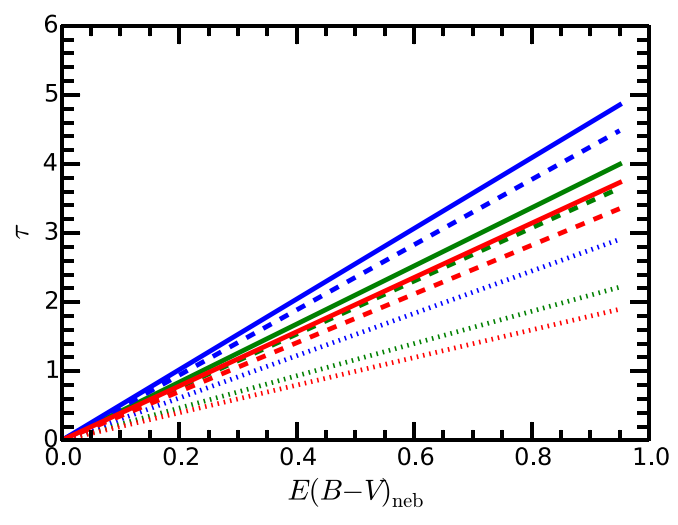


Figure 2. Optical depth (τ) of H ϵ (solid lines), H γ (dashed lines), and H α (dotted lines) vs. $E(B-V)_{\rm neb}$ for the Calzetti et al. (2000) attenuation curve (blue), SMC extinction curve (red), and MW curve (green).

identified nine samples of galaxies with unique combinations of Balmer emission lines with spectral coverage. The characteristics of these samples are listed in Table 2, including the number of galaxies belonging to each sample, the redshift range and mean redshift of galaxies in each sample, and the fluxes of the covered emission lines that all galaxies in each sample have in common. Because the calculated $H\epsilon$ flux depends on that measured for [Ne III] $\lambda 3870$ (Section 2.6), a galaxy is considered to have coverage of $H\epsilon$ only if it also has coverage of [Ne III] $\lambda 3870$.

In constructing these samples, we required that the longest-wavelength line with coverage, namely $H\alpha$, be detected with $S/N \geqslant 3$, so that the individual galaxy spectra may be normalized by the $H\alpha$ flux when calculating the composite spectrum (Section 2.5). There is no requirement for coverage placed on lines that have blank entries in Table 2. As such, the different samples listed in Table 2 have, in general, many galaxies in common. For example, sample S3 consists of all galaxies in sample S2 that have coverage of $H\epsilon$, in addition to all lines required to be covered in S2. The last column of Table 2 indicates for each sample all of the other samples of which it is a subset. In total, we used 532 galaxies from the MOSDEF sample to constrain the shape of the nebular attenuation curve.

Composite spectra were constructed for each of the nine samples listed in Table 2. For each composite, we measured the covered Balmer emission lines associated with the corresponding sample. These measurements were used to compute the shape of the nebular attenuation curve for each sample, as discussed in the next section.

4. Calculation of the Shape of the Nebular Attenuation Curve

The relationship between the observed (or attenuated) and intrinsic fluxes of a line centered at wavelength λ , denoted by

 $f(\lambda)$ and $f_0(\lambda)$, respectively, can be expressed as follows:

$$f(\lambda) = f_0(\lambda) \times 10^{-0.4A(\lambda)},\tag{1}$$

where $A(\lambda)$ is the attenuation in magnitudes at wavelength λ . For any two lines centered at wavelengths λ_1 and λ_2 , we can then write

$$\frac{f(\lambda_{\rm I})}{f(\lambda_2)} = \frac{f_0(\lambda_{\rm I})}{f_0(\lambda_2)} \times 10^{-0.4[A(\lambda_{\rm I}) - A(\lambda_2)]},\tag{2}$$

or

$$A(\lambda_2) = 2.5 \left[\log_{10} \left(\frac{f(\lambda_1)}{f(\lambda_2)} \right) - \log_{10} \left(\frac{f_0(\lambda_1)}{f_0(\lambda_2)} \right) \right] + A(\lambda_1).$$
(3)

In our analysis, λ_1 denotes the wavelength of the reddest line with coverage, namely H α (Table 2). We define a new quantity,

$$A'(\lambda_2) \equiv A(\lambda_2) + [1 - A(\lambda_1)]$$

$$= 2.5 \left[\log_{10} \left(\frac{f(\lambda_1)}{f(\lambda_2)} \right) - \log_{10} \left(\frac{f_0(\lambda_1)}{f_0(\lambda_2)} \right) \right] + 1, \quad (4)$$

which is equivalent to $A(\lambda_2)$ for $A(\lambda_1) = 1$ and depends only on measured line flux ratios. With these definitions, there is an offset between $A'(\lambda_2)$ and $A(\lambda_2)$, $1 - A(\lambda_1)$, that is constant and independent of λ_2 . The intrinsic Balmer emission line ratios (Table 1), along with the observed ratios measured from the composites constructed for the samples listed in Table 2, were used with Equation (4) to compute $A'(\lambda_2)$. We then fit $A'(\lambda_2)$ versus λ_2 using linear and quadratic polynomials of the $A'(\lambda) = a_0 + a_1/\lambda$ (linear in $1/\lambda$) $A'(\lambda) = a_0 + a_1/\lambda + a_2/\lambda^2$ (quadratic in $1/\lambda$), respectively, where λ is the wavelength in μ m. While the quadratic-in-1/ λ form results in reduced χ^2 that are typically an order of magnitude smaller than those obtained with the linear-in-1/ λ form, we present results using both forms to demonstrate the degree to which the functional fit affects the derived attenuation curve. Our measurements lack sufficient precision and wavelength sampling to warrant more complicated functional forms for the wavelength dependence of the attenuation curve.

The attenuation curve is defined as

$$k(\lambda) \equiv \frac{A(\lambda)}{E(B-V)},$$
 (5)

where E(B-V) = A(B) - A(V) is the reddening in magnitudes. As we are concerned with the nebular attenuation curve, E(B-V) is the reddening appropriate to the ionized gas, $E(B-V)_{\text{neb}}$. Taking the effective wavelengths of the *B* and *V* bands to be 4400 and 5500 Å, respectively, we can then define an attenuation curve that is related to $A'(\lambda_2)$,

$$k'(\lambda) = \frac{A'(\lambda)}{A'(4400 \text{ Å}) - A'(5500 \text{ Å})},\tag{6}$$

where we have set $\lambda = \lambda_2$ for simplicity. Given the previous definitions, the offset between $k'(\lambda)$ and $k(\lambda)$ is $[1 - A(\lambda_1)]/E(B - V)_{\text{neb}}$ and is independent of λ .

 $[\]overline{^{13}}$ The MOSDEF sample includes a number of galaxies at $z\gtrsim 3$ that do not have coverage of $\mathrm{H}\alpha$ but do have high-S/N detections of $\mathrm{H}\beta$. While the attenuation curve can, in principle, be derived for these galaxies, we chose not to include them in our analysis, as the lack of $\mathrm{H}\alpha$ coverage results in larger uncertainties in $E(B-V)_{\mathrm{neb}}$ and, consequently, the shape of the attenuation curve.

Table 2 Samples, Balmer Emission Line Coverage, and Line Flux Ratios^a

Sample	$N^{\mathbf{b}}$	z Range $(\langle z \rangle)^c$	$H\alpha$	Ηβ	$H\gamma$	$H\delta$	$H\epsilon^{d}$	Subset of ^e
S1	240	1.2467-2.6403 (1.9424)	1.000 ± 0.004	0.234 ± 0.004	0.085 ± 0.004	•••	•••	
S2	130	1.3631-2.6196 (1.5875)	1.000 ± 0.004	0.224 ± 0.004	0.085 ± 0.004	0.038 ± 0.004		S1, S7
S3	72	1.5031-2.1230 (1.6719)	1.000 ± 0.005	0.225 ± 0.006	0.076 ± 0.006	0.033 ± 0.005	0.020 ± 0.007	S1-S2, S4-S9
S4	355	1.5031-2.4225 (2.1041)	1.000 ± 0.003	0.247 ± 0.003			0.024 ± 0.004	
S5	80	1.5031-2.4225 (1.7433)	1.000 ± 0.005	0.227 ± 0.006	0.077 ± 0.006	•••	0.021 ± 0.007	S1, S4
S6	278	1.5031-2.3104 (2.0384)	1.000 ± 0.003	0.247 ± 0.003		0.044 ± 0.003	0.023 ± 0.004	S4, S9
S7	141	1.3549-2.6196 (1.6206)	1.000 ± 0.004		0.085 ± 0.004	0.038 ± 0.004		
S8	82	1.5031-2.1244 (1.7213)	1.000 ± 0.005		0.077 ± 0.006	0.033 ± 0.005	0.019 ± 0.007	S7, S9
S 9	289	1.5031–2.3104 (2.0401)	1.000 ± 0.003	•••	•••	0.044 ± 0.003	0.022 ± 0.004	

Notes.

Accordingly, determining $k'(\lambda)$ is effectively equivalent to determining $k(\lambda)$ up to a normalization constant (Section 5.2).

In summary, we used the observed and intrinsic Balmer emission line ratios to compute $A'(\lambda_2)$ using Equation (4), fit linear and quadratic polynomials to $A'(\lambda_2)$, used these polynomial fits to determine the values of A'(4400 Å) and A'(5500 Å), and used Equation (6) to calculate $k'(\lambda)$. As noted above, $k'(\lambda)$ is equivalent to $k(\lambda)$ apart from a normalization constant. Measurement uncertainties were propagated throughout these calculations, such that the final uncertainty in a given $k'(\lambda)$ point includes uncertainty in line flux measurements, slit loss corrections for those line ratios where the two lines were observed in different bands, ¹⁴ and $E(B-V)_{\text{neb}}$. All of the $k'(\lambda)$ points determined for individual samples were then fit together, weighted by their inverse variances, using the polynomial forms discussed above to produce a final attenuation curve. In practice, the final attenuation curve was determined using $k'(\lambda)$ points from only those lines that had $S/N \geqslant 3$.

Because there are many galaxies in common between the samples listed in Table 2 (Section 3), the $k'(\lambda)$ points computed from these samples are not completely independent of each other. Thus, the formal uncertainty in the fit to $k'(\lambda)$ will underestimate the true measurement uncertainty. To determine the error in the fit to $k'(\lambda)$, the samples were restricted so that all galaxies in each sample have exactly the same set of covered emission lines (i.e., any galaxies that have coverage of lines with blank entries in Table 2 are excluded from the samples). With this requirement, the individual samples do not have any galaxies in common and will contain fewer galaxies than indicated in Table 2; all but five samples (S1, S2, S3, S4, and S6) contain fewer than 10 galaxies. The $k'(\lambda)$ points from these five samples were fit using linear and

quadratic polynomials as described above, and we adopted the formal uncertainty on these fits as representative of the actual measurement uncertainty in the mean nebular attenuation curve. The functional forms of $k'(\lambda)$ versus $1/\lambda$ are

$$k_{\rm L}'(\lambda) = -2.479 + \frac{2.286}{\lambda}$$
 (7)

for the linear-in- $1/\lambda$ fit and

$$k_{\rm Q}'(\lambda) = 2.074 - \frac{2.519}{\lambda} + \frac{1.196}{\lambda^2}$$
 (8)

for the quadratic-in-1/ λ fit for 0.38 μ m $\lesssim \lambda \lesssim 0.66 \mu$ m. The curves have been shifted in normalization so that $k'_{L,Q}(H\alpha) = 1$. The subscripts "L" and "Q" refer to the linear-in-1/ λ and quadratic-in-1/ λ forms, respectively, and are used to distinguish the curves found here from other common extinction/attenuation curves.

5. Results

The attenuation curve derived here is shown in Figure 3, along with the MW, Calzetti et al. (2000), and Small Magellanic Cloud (SMC) curves, all shifted in normalization so that $k'(H\alpha)_{MW,Calz,SMC} = k'_{L,O}(H\alpha)$. The MW (Galactic extinction) curve is most commonly used to derive the nebular reddening and dust corrections to nebular lines, while the Calzetti et al. (2000) and SMC curves are typically assumed for the reddening of the stellar continuum in high-redshift galaxies. In what follows, we compare the curve found here with the Galactic extinction curve and several other commonly used extinction/attenuation curves.

5.1. Shape of the Average Nebular Attenuation Curve

Our results imply that the shape of the nebular attenuation curve is similar to that of the MW within the uncertainties, irrespective of the functional (linear or quadratic) form adopted for the curve, as shown in Figure 3. This figure also highlights the systematic uncertainty stemming from the adopted functional form for $k'(\lambda)$. Specifically, $k'(\lambda)$ depends on $E(B-V)_{\text{neb}}$, and $E(B-V)_{\text{neb}}$ is derived from a polynomial

a Sample characteristics and line fluxes relative to H α . For each sample, flux measurements are included only for those lines that have $S/N \geqslant 3$ in the composite spectrum and coverage for all galaxies in that sample. Only lines that satisfy these requirements are used to compute the attenuation curve for each sample. Number of galaxies in the sample.

c Redshift range and mean redshift (in parentheses) of galaxies in the sample. Because of the multimodal redshift distributions of some of the samples, there may be

few galaxies that lie at the mean redshift of galaxies in the sample. d A galaxy is considered to have coverage of H ϵ only if its spectrum also includes [Ne III] $\lambda 3870$, as the latter was used to estimate the contribution of [Ne III] $\lambda 3969$ to the H ϵ + [Ne III] λ 3969 blend (Section 2.6). The H ϵ /H α line flux ratios reported in this column are corrected for the contribution of [Ne III] λ 3969. e Indicates the samples of which this sample is a subset.

The random uncertainty in a line flux ratio due to slit loss corrections, where the two lines were observed in different bands, is \sim 18% (see Section 2.2). The total uncertainty due to slit loss corrections when measuring lines in the composite spectra is set equal to $18\%\sqrt{N_1}/N_2$, where N_1 is the number of objects contributing to the composite for which the two lines of the line ratio are covered in different filters and N_2 is the total number of objects contributing to the composite.

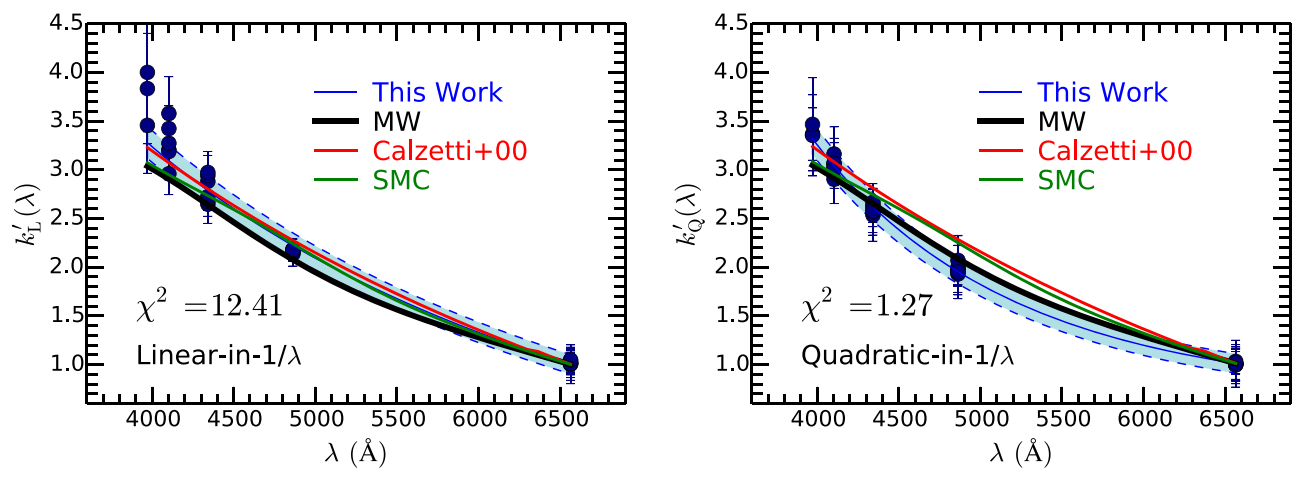


Figure 3. Shown is $k'(\lambda)$ vs. λ for the linear-in-1/ λ (left) and quadratic-in-1/ λ polynomial forms (right). Measurements are shown by the blue circles; these values differ between the two polynomial forms, since $k'(\lambda)$ depends on $E(B-V)_{\text{neb}}$ and the latter depends on the functional form used to fit $A'(\lambda)$. Error bars for each $k'(\lambda)$ point are also shown. The best-fit polynomial and 95% confidence intervals are denoted by the solid and dashed blue lines, respectively. The reduced χ^2 for the fits are indicated in each panel. For comparison, the MW extinction curve, shifted so that its value at the wavelength of H α is equal to that of the curve derived here, is shown by the thick black line. Similarly, the shifted SMC and Calzetti et al. (2000) curves are shown by the solid green and red lines, respectively.

fit to $A'(\lambda)$ (Section 4). The linear-in- $1/\lambda$ fit to $A'(\lambda)$ results in an $E(B-V)_{\rm neb}$ that is $\approx 17\%$ smaller than that derived from the quadratic-in- $1/\lambda$ fit. As a result, the $k'(\lambda)$ points for the linear-in- $1/\lambda$ function are the same percentage larger than those derived for the quadratic-in- $1/\lambda$ function.

While this systematic uncertainty does not change our conclusion that the curve found here is similar to the Galactic extinction curve, it does affect the comparison of the curve to those that are commonly adopted to dust-correct the stellar continuum emission in galaxies. In particular, the simple linear-in-1/ λ form implies a nebular attenuation curve that is indistinguishable in shape from other common curves at rest-frame optical wavelengths. On the other hand, adopting the quadratic-in-1/ λ form yields a nebular attenuation curve that has more curvature than other common curves at rest-frame optical wavelengths.

There are a couple of reasons why the quadratic-in-1/ λ form may be preferred. First, this functional form yields a significantly lower reduced χ^2 than the linear-in-1/ λ form. The latter predicts lower values of $k'(\lambda)$ at $\lambda \lesssim 4500$ Å, relative to $H\alpha$, than what the shorter-wavelength Balmer lines suggest. Second, most of the common extinction/attenuation curves found in the literature (e.g., Cardelli et al. 1989; Calzetti et al. 2000; Gordon et al. 2003) require a higher-order polynomial to fully capture their shape at rest-frame optical wavelengths, in contrast to the longer-wavelength ($\lambda \gtrsim 7000 \text{ Å}$) behavior that is typically parameterized by an inverse power law in λ . Precise measurements of even higher-order Balmer lines and lines of the Paschen series, as well as the underlying stellar absorption, will clarify the functional form of the nebular attenuation curve over a broader range of wavelengths than is currently accessible. Finally, whether the aforementioned similarities and differences between the various curves extend to the reddening at UV wavelengths where the variations between extinction/attenuation curves are more pronounced remains unknown.

5.2. Normalization of the Average Nebular Attenuation Curve

The normalization of the total nebular dust attenuation curve, $k(\lambda)$, may be found by extrapolating $k'(\lambda)$ to some sufficiently

long wavelength and setting the curve to be zero at this point (e.g., Reddy et al. 2015). The MW, SMC, and LMC curves all become very close to zero at $\lambda \gtrsim 2.8~\mu m$. Extrapolating Equation (7) to $2.8~\mu m$ and forcing the value to be zero at this point implies the following total attenuation curve for the linear-in- $1/\lambda$ fit:

$$k_{\rm L}(\lambda) = -0.816 + \frac{2.286}{\lambda},$$

 $0.40 \le \lambda \le 0.66 \ \mu \rm m.$ (9)

A similar normalization of the quadratic-in- $1/\lambda$ fit requires one to force $k_Q'(\lambda)$ (Equation (8)) to conform to the commonly adopted behavior where $k(\lambda) \propto 1/\lambda$ as $\lambda \to \infty$. Thus, we shifted $k_Q'(\lambda)$ to have the same value as $k_L(\lambda)$ at 0.66 μ m to ensure a continuous function, thus obtaining the following total attenuation curve for the quadratic-in- $1/\lambda$ fit:

$$k_{Q}(\lambda) = 3.719 - \frac{2.519}{\lambda} + \frac{1.196}{\lambda^{2}},$$

$$0.40 \le \lambda \le 0.66 \,\mu\text{m};$$

$$= -0.816 + \frac{2.286}{\lambda},$$

$$\lambda > 0.66 \,\mu\text{m}.$$
(10)

The extrapolation of the total attenuation curve redward of $\lambda=0.66~\mu\mathrm{m}$ should be used with caution given that $k_{\mathrm{L}}(\lambda)$ is constrained only using points blueward of this limit. The ratio of the total-to-selective absorption at the V band is $R_V=3.34$ and 3.09 for the linear and quadratic forms of the total attenuation curve, respectively. The difference between these values (δ $R_V\simeq0.2$) gives an estimate of the systematic uncertainty in R_V that stems from assuming different functional forms of $k(\lambda)$ versus λ at long wavelengths. There is additional uncertainty associated with the specific wavelength at which the attenuation curve is forced to zero. For example, the difference in R_V obtained when assuming a "zero wavelength" of 3.0 μ m rather than 2.8 μ m is δ $R_V\simeq0.05$. The values of R_V obtained here are entirely consistent with that of the Galactic

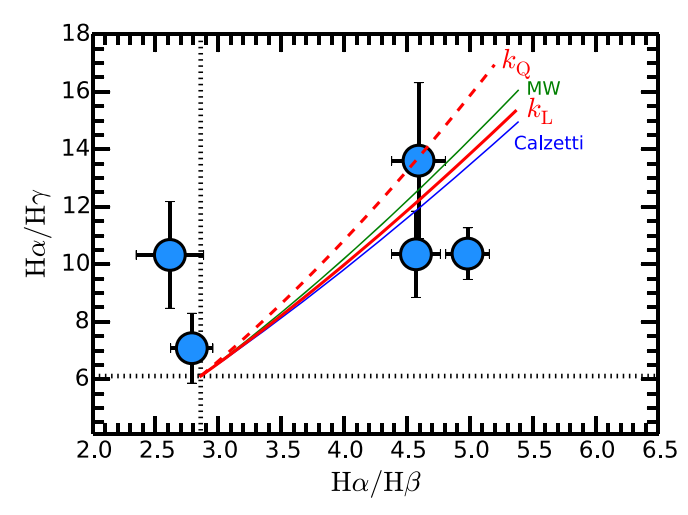


Figure 4. Ratios of $H\alpha/H\gamma$ vs. $H\alpha/H\beta$ for five galaxies where $H\alpha$, $H\beta$, and $H\gamma$ are detected with $S/N \geqslant 5$ (points). The relationships between these ratios for different attenuation curves are indicated by the curves, including the linear and quadratic forms given by Equations (9) and (10), where reddening increases toward the upper right-hand side of the figure. The SMC curve lies very close to that of the Calzetti et al. (2000) curve, and the Reddy et al. (2015) curve lies very close to $k_L(\lambda)$. The dotted lines indicate the intrinsic line ratios. The two objects whose ratios lie below the intrinsic values are consistent within 3σ with having very little reddening.

extinction curve ($R_V = 3.1$; Cardelli et al. 1989) given the aforementioned systematic errors.

5.3. Balmer Emission Line Ratios of Individual Galaxies

There are a handful of galaxies where the higher-order Balmer emission lines (e.g., $H\gamma$ and $H\delta$) are detected in individual spectra. The joint uncertainties in the resulting multiple Balmer emission line ratios (i.e., $H\alpha/H\beta$, $H\alpha/H\gamma$, etc.) are such that we cannot rule out any of the nebular duta attenuation curves described above. Figure 4 shows the $H\alpha/H\beta$ and $H\alpha/H\gamma$ ratios of the five galaxies in our sample where $H\alpha$, $H\beta$, and $H\gamma$ are detected with $S/N \geqslant 5$, relative to how these ratios depend on each other for different attenuation/extinction curves. These measurements were made by simultaneously fitting the stellar continuum from the best-fit SED model with the spectra of the individual line detections, thus accounting for underlying Balmer absorption. On average, the measurements are consistent within the errors with all of the aforementioned extinction/attenuation curves.

6. Discussion

The nebular attenuation curve has an important bearing on the derivation of a number of fundamental physical properties of galaxies and the ISM contained within them. Our results imply a nebular attenuation curve that is similar to the Galactic extinction curve within the random and systematic uncertainties discussed above. Here we consider the nebular reddening of galaxies in our sample, how the nebular reddening compares to the reddening of the stellar continuum, and how differences between the two values of reddening may be interpreted in the context of recent advancements in stellar population synthesis modeling.

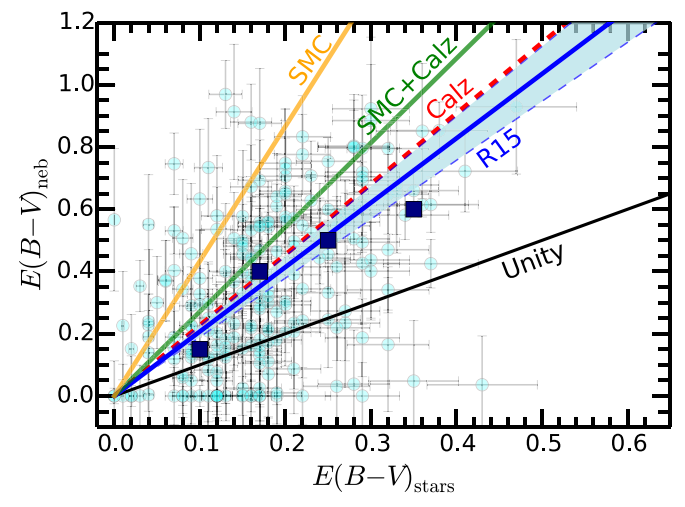


Figure 5. Nebular reddening, derived assuming the $k_Q(\lambda)$ parameterization of the nebular attenuation curve, vs. the reddening of the stellar continuum for individual galaxies (circles) with the fiducial modeling described in Section 2.4, i.e., assuming the Reddy et al. (2015) attenuation curve. The large squares indicate the average $E(B-V)_{\rm neb}$ determined from composite spectra that were constructed in bins of $E(B-V)_{\rm stars}$ and include objects where $H\beta$ is not significantly detected. The one-to-one (unity) relation is shown by the black line. The best-fit linear relation to individual points and 95% confidence intervals are indicated by the solid blue line and shaded regions, respectively. Additionally, we show the relations obtained if we assume the Calzetti et al. (2000) relation (dashed red line), an SMC extinction curve (solid orange line), and combined modeling that assumes the SMC and Calzetti et al. (2000) curves for low- and high-mass galaxies, respectively (see text). In all cases, we find that $E(B-V)_{\rm neb}$ is larger than $E(B-V)_{\rm stars}$, on average.

6.1. Reddening Comparisons

The nebular reddening, $E(B-V)_{\text{neb}}$, can be derived from the Balmer decrement, $H\alpha/H\beta$, as follows:

$$E(B-V)_{\text{neb}} = \frac{2.5}{k(H\beta) - k(H\alpha)} \log_{10} \left[\frac{H\alpha/H\beta}{2.86} \right]. \quad (11)$$

The similarities between the nebular attenuation curve found here and the Galactic extinction curve imply that the corresponding $E(B-V)_{\rm neb}$ values are also similar. Motivated by the expected correlation between the reddening of the ionized gas and stellar continuum in galaxies (e.g., Fanelli et al. 1988; Calzetti 1997; Calzetti et al. 2000; Kreckel et al. 2013), we recomputed the relationship between $E(B-V)_{\rm neb}$ and $E(B-V)_{\rm stars}$, where the former was computed assuming $k_{\rm Q}(\lambda)$ and the latter was determined from SED fitting for our fiducial assumptions of the solar-metallicity BC03 models and the Reddy et al. (2015) stellar attenuation curve (Section 2.4). Figure 5 shows the comparison between the reddenings for galaxies with $S/N \geqslant 5$ in both $H\alpha$ and $H\beta$ and where $E(B-V)_{\rm neb} \leqslant 1.0$.

A Spearman correlation test indicates that $E(B-V)_{\text{neb}}$ is correlated with $E(B-V)_{\text{stars}}$ with $\simeq 8\sigma$ significance, and linear regression between the two variables (keeping the intercept fixed at zero) gives the following relation:

$$E(B - V)_{\text{neb}} = (2.070 \pm 0.088) \times E(B - V)_{\text{stars}}.$$
 (12)

The trend between $E(B-V)_{\rm neb}$ and $E(B-V)_{\rm stars}$ is not significantly affected when accounting for galaxies that have undetected H β lines (S/N < 3) based on stacking in bins of $E(B-V)_{\rm stars}$ (Figure 5).

The data indicate a relationship between nebular and stellar reddening that is similar in slope to the canonical relation from (2000),al. $E(B-V)_{\text{neb}} = 2.27 \times E(B-V)_{\text{stars}}$. Figure 5 shows the relations between $E(B-V)_{\text{neb}}$ and $E(B-V)_{\text{stars}}$ when assuming other stellar attenuation curves for deriving $E(B-V)_{\text{stars}}$. For example, Shivaei et al. (2020) found that MOSDEF galaxies in the upper ~half of the stellar mass distribution $(M_* \gtrsim 10^{10.4} M_{\odot})$ have a shallower (Calzetti-like) stellar attenuation curve, while those in the lower ~half of the mass distribution have a steeper (SMC-like) curve. These results are consistent with other studies that have found steeper curves for high-redshift ($z \gtrsim 2$) galaxies with lower stellar masses (e.g., Reddy et al. 2006, 2010, 2012a; Bouwens et al. 2016; Fudamoto et al. 2017, 2020). Based on these previous studies, we also modeled the galaxies assuming the SMC extinction curve with the $0.2\,Z_{\odot}$ metallicity models for those with $E(B - V)_{\text{neb}} \leq 0.4$ (corresponding to $M_* \lesssim 10^{10.4} M_{\odot}$; Shivaei et al. 2020) and the Calzetti et al. (2000) curve with the Z_{\odot} metallicity models for those with $E(B-V)_{\rm neb} > 0.4$. The resulting trend between $E(B-V)_{neb}$ and $E(B-V)_{stars}$ is indicated by the green line in Figure 5 ("SMC+Calz" trend). Finally, we show the trend obtained if we assume the SMC extinction curve for all galaxies in our sample.

The average ratios between the nebular and stellar reddening are $\langle E(B-V)_{\text{neb}}/E(B-V)_{\text{stars}}\rangle = 2.070, 2.273, 2.712,$ and 4.331 for the Reddy et al. (2015), Calzetti et al. (2000), SMC +Calz, and SMC curves, respectively. The ratio increases with the steepness of the assumed stellar attenuation curve because assuming such a curve results in smaller $E(B - V)_{\text{stars}}$. More generally, the specific relationship between $E(B - V)_{neb}$ and $E(B-V)_{\text{stars}}$ is of limited value without knowledge of the attenuation curves used to derive the color excesses (e.g., Reddy et al. 2015; Theios et al. 2019; Shivaei et al. 2020). Furthermore, as is evident from Figure 5, the relatively large scatter between $E(B-V)_{\text{neb}}$ and $E(B-V)_{\text{stars}}$ (rms $\simeq 0.22$) —in conjunction with the fact that they are derived assuming a fixed average dust curve that may not apply on a galaxy-bygalaxy basis—implies that the average relationship between the two is only meaningful in the context of large ensembles of galaxies rather than individual objects (Reddy et al. 2015; Theios et al. 2019; Shivaei et al. 2020). At any rate, in all cases of the assumed attenuation curves, we find that the reddening of the nebular lines exceeds that of the stellar continuum, on average.

From a physical standpoint, the increased reddening toward the ionized regions of high-redshift galaxies implies that the youngest stellar populations are enshrouded by a higher column density and/or covering fraction of dust. We return to this issue in Section 6.2.

6.2. A Physical Context for the Difference between Nebular and Stellar Reddening

One of the key results of our analysis is that the Balmer decrements of typical star-forming galaxies at $z\sim 2$ imply nebular color excesses that are significantly redder than those measured for the stellar continuum (Figure 5). This conclusion is reached irrespective of the attenuation curve assumed for either the nebular regions or the stellar continuum. This differential reddening has been noted in several other studies of high-redshift galaxies (e.g., Förster Schreiber et al. 2009; Reddy et al. 2010; Kashino et al. 2013; Price et al. 2014; Reddy

et al. 2015; Shivaei et al. 2020) and is also seen in local starforming galaxies (e.g., Fanelli et al. 1988; Calzetti 1997; Calzetti et al. 2000; Kreckel et al. 2013). From a physical standpoint, the discrepancy between the nebular and stellar reddening has generally been attributed to the redder lines of sight toward the youngest stellar populations in a galaxy (e.g., Fanelli et al. 1988; Calzetti 1997; Calzetti et al. 2000; Kreckel et al. 2013). Here we revisit the physical context for the difference in reddening of the nebular emission lines and stellar continuum in light of recent improvements in stellar population modeling that account for the effects of binary stellar evolution.

The simplest interpretation for the difference in the reddening of the nebular emission lines and stellar continuum in galaxies is based on considering the crossing times and/or dissipation timescales for molecular clouds. Specifically, the main-sequence lifetimes of the very massive single nonrotating stars that dominate the Balmer emission line luminosities (spectral type O6 and earlier; Leitherer 1990) are shorter than the typical molecular cloud crossing timescale of $\simeq 1-3$ Myr (Calzetti et al. 1994). Thus, these very massive stars are producing most of the ionizing flux while they are still embedded in their birth clouds and in regions of higher dust column density. This prodigious source of ionizing photons is lost once these massive stars go supernova, and the molecular cloud is subsequently disrupted. Those OB associations that are observed after their clouds have dissipated and lack the most massive O stars produce fewer ionizing photons and do not contribute as much to the Balmer emission lines, while still contributing significantly to the nonionizing stellar continuum. Hence, the Balmer lines primarily originate from regions around the most massive stars that are subject to additional reddening beyond that affecting the stellar continuum.

Here we reevaluate the picture described above in the context of recent studies that demonstrate the necessity of binary stellar populations (or rotating massive stars) to jointly reproduce the rest-frame UV and optical spectra of typical galaxies at $z \sim 2$. Specifically, several studies argue that low stellar metallicity massive binary stellar populations are required to reproduce the observed strong line ratios (e.g., $[O III]/H\beta$ versus $[N II]/H\alpha)$ of $z \sim 2$ galaxies while simultaneously matching the rest-frame far-UV spectra (e.g., Steidel et al. 2014, 2016; Topping et al. 2020). Three consequences of these massive binary star models are that they increase massive star main-sequence lifetimes, result in a broader range of stellar masses over which ionizing photon production occurs, and boost the ionizing flux per unit SFR (Eldridge et al. 2017). At subsolar stellar metallicities ($Z \leq 0.3Z_{\odot}$), these models predict an H-ionizing flux that peaks roughly 3 Myr-and falls by a factor of ≈3 roughly 10 Myr—after an instantaneous burst of star formation (Stanway et al. 2016). Such models also produce a factor of $\gtrsim 5 \times$ the ionizing flux of single star models 10 Myr after an initial burst of star formation.

The increase in and duration of ionizing flux production predicted by these models suggest that significant ionizing flux may persist even after an OB association drifts away from the parent giant molecular cloud (GMC) on a timescale of \lesssim 3 Myr. Once the massive stars are free from the obscuring dust

 $[\]overline{^{15}}$ For a fixed initial mass function, metallicity, star formation history, and age, stellar population synthesis models that include the effects of binary evolution yield higher ionizing fluxes than single star models, but the shape of the nonionizing UV continuum is very similar between the two. As $E(B-V)_{\text{stars}}$ is determined from the nonionizing UV continuum, these values are largely insensitive to the effects of binary stellar evolution.

associated with their natal clouds, the line emission from the nebulae surrounding these stars would be subject to essentially the same columns of dust that affect the stellar continuum, resulting in a nebular reddening that is more in line with that measured for the stellar continuum. The observed differences between the nebular and stellar reddening suggest that the molecular cloud crossing timescales may be at least a factor of $3 \times$ longer than those of local GMCs and closer to the typical cloud disruption timescales of $\simeq 10-30$ Myr (Blitz & Shu 1980; McKee & Ostriker 2007).

A second likely possibility for the differential reddening between the nebular lines and stellar continuum is related to the constant or rising star formation histories that are favored for typical star-forming galaxies at $z \gtrsim 2$ (e.g., Papovich et al. 2011; Reddy et al. 2012b). For these star formation histories, the lower ionizing flux of slightly older OB associations that are dissociated from their birth clouds will be compensated by the higher ionizing flux of newly formed and dustier OB associations, where the latter will contribute significantly to the galaxy-averaged $E(B-V)_{\rm neb}$.

A third and equally likely possibility is that the dust that reddens the Balmer line photons may not be localized to the molecular clouds but distributed more widely in the ISM, i.e., in the ionized and neutral gas phases. In this case, even after the parent molecular cloud has dissipated, the nebular line emission may be dominated by those recently exposed OB associations that are still located preferentially in regions of higher dust column density as averaged over all phases of the ISM. Indeed, modeling of the far-UV spectra of $z \sim 3$ galaxies suggests that a significant fraction of dust is not associated with the molecular phase of the ISM in these galaxies (Reddy et al. 2016). This conclusion is consistent with the almost ubiquitous presence of metals (and hence dust) in the neutral and ionized ISM as indicated by low- and high-ionization interstellar metal absorption lines in the rest-frame far-UV spectra of highredshift galaxies (e.g., Shapley et al. 2003).

In general, the limited spatial resolution characteristic of high-redshift galaxy observations implies that global line and continuum measurements undoubtedly include many OB associations. Thus, the difference in $E(B-V)_{neb}$ and $E(B-V)_{\text{stars}}$ (or their similarity for some subsets of highredshift galaxies; e.g., Reddy et al. 2010, 2015; Pannella et al. 2015; Shivaei et al. 2020) is likely driven by the distribution of dust column densities along the lines of sight to different OB associations. Determining which of the above possibilities, if any, may be most relevant for explaining the degree of difference in the reddening of the nebular lines and stellar continuum will require detailed simulations of small-scale star formation, associated feedback, dust formation, and the subsequent evolution of the GMCs when adopting stellar population models that include the effects of stellar multiplicity.

7. Conclusions

We use deep rest-frame optical spectra of 532 star-forming galaxies at redshifts $z \simeq 1.4$ –2.6 from the MOSDEF survey to place the first constraints on the nebular attenuation curve at high redshift. Specifically, we use the first five low-order Balmer emission lines (H α , H β , H γ , H δ , and H ϵ) detected in the composite spectra of these galaxies to infer the shape and normalization of the nebular attenuation curve at rest-frame optical wavelengths.

The nebular attenuation curve derived here is similar in shape to that of the Galactic extinction curve at rest-frame optical wavelengths, a result that is insensitive to the functional form assumed for the curve (Section 5.1; Figure 3). The derived ratio of the total-to-selective absorption at the V band depends on the extrapolation of the nebular attenuation curve to long wavelengths and lies in the range $R_V \approx 3.1$ –3.3. Within the systematic uncertainties, these values of R_V are similar to the $R_V = 3.1$ for the Galactic extinction curve (Section 5.2). If the similarity in shape and normalization of the attenuation curve extends to rest-frame UV wavelengths, then our results suggest that the dust "seen" along the nebular sight lines in $z \sim 2$ galaxies can be approximated as a foreground screen of dust that has similar grain scattering/absorption properties and size distribution as those inferred for the average Galactic sight line.

If we assume the stellar attenuation curve of Reddy et al. (2015), we obtain a relationship between $E(B-V)_{\rm neb}$ and $E(B-V)_{\rm stars}$ that is similar in slope to that of the commonly assumed Calzetti et al. (2000) relation (Section 6.1). The exact slope will, of course, depend on the choice of stellar attenuation curve: steeper curves result in higher slopes and higher average ratios of nebular-to-stellar reddening. Regardless of the adopted curve for the stellar continuum, however, we find that the nebular reddening is, on average, larger than that of the stellar continuum.

We discuss the physical context for this differential reddening of the nebular lines and stellar continuum in light of recent results that favor binary population synthesis models in reproducing the rest-frame UV and optical spectra of high-redshift galaxies. These models predict ionizing photon fluxes that are a few times larger, and can be sustained for longer periods, relative to those obtained from single star models. In this framework, the difference in reddening of the nebular lines and stellar continuum may imply molecular cloud crossing times in excess of a few Myr, SFRs that are constant or increase with time such that newly formed (and dustier) OB associations always dominate the total ionizing flux, or that the dust that dominates the reddening of the Balmer lines is associated with the nonmolecular (i.e., neutral and ionized) phases of the ISM (Section 6.2).

The analysis presented here hints at the rich array of studies that will be enabled with direct measurements of multiple lowand high-order nebular recombination emission lines for individual galaxies with the next generation of ground- (e.g., ≥30 m class) and space-based (e.g., James Webb Space Telescope) facilities. The effective depths of the composite spectra used here to constrain the nebular attenuation curve have limited our analysis to an examination of the average shape and normalization of the dust curve across our entire sample. Aside from enabling nebular dust corrections on an object-by-object basis, direct detections of the higher-order Balmer lines and longer-wavelength Paschen and Brackett lines, along with constraints from the rest-frame UV (e.g., He II recombination lines), will allow for analyses of how the normalization and shape of the curve vary from galaxy to galaxy and how the curve may depend on metallicity, stellar mass, SFR, and other characteristics. Such analyses will provide a powerful new probe of the life cycle, properties, and spatial distribution of dust in galaxies.

We acknowledge support from NSF AAG grants AST-1312780, 1312547, 1312764, and 1313171; archival grant AR-

13907, provided by NASA through the Space Telescope Science Institute; and grant NNX16AF54G from the NASA ADAP program. We are grateful to the MOSFIRE instrument team for building this powerful instrument and to Marc Kassis at the Keck Observatory for his many valuable contributions to the execution of the MOSDEF survey. We also acknowledge the 3D-HST collaboration, who provided us with spectroscopic and photometric catalogs used to select MOSDEF targets and derive stellar population parameters. We also thank I. McLean, K. Kulas, and G. Mace for taking observations for the MOSDEF survey in 2013 May and June. We wish to extend special thanks to those of Hawaiian ancestry on whose sacred mountain we are privileged to be guests. Without their generous hospitality, the observations presented herein would not have been possible.

ORCID iDs

Naveen A. Reddy https://orcid.org/0000-0001-9687-4973
Alice E. Shapley https://orcid.org/0000-0003-3509-4855
Mariska Kriek https://orcid.org/0000-0002-7613-9872
Charles C. Steidel https://orcid.org/0000-0002-4834-7260
Irene Shivaei https://orcid.org/0000-0003-4702-7561
Ryan L. Sanders https://orcid.org/0000-0003-4792-9119
Alison L. Coil https://orcid.org/0000-0002-2583-5894
Brian Siana https://orcid.org/0000-0002-4935-9511
William R. Freeman https://orcid.org/0000-0003-3559-5270

Mojegan Azadi https://orcid.org/0000-0001-6004-9728
Tara Fetherolf https://orcid.org/0000-0002-3551-279X
Gene Leung https://orcid.org/0000-0002-9393-6507
Sedona H. Price https://orcid.org/0000-0002-0108-4176

References

```
Azadi, M., Coil, A., Aird, J., et al. 2018, ApJ, 866, 63
Azadi, M., Coil, A. L., Aird, J., et al. 2017, ApJ, 835, 27
Blitz, L., & Shu, F. H. 1980, ApJ, 238, 148
Bouwens, R. J., Smit, R., Labbé, I., et al. 2016, ApJ, 831, 176
Bruzual, G., & Charlot, S. 2003, MNRAS, 344, 1000
Buat, V., Boquien, M., Małek, K., et al. 2018, A&A, 619, A135
Calzetti, D. 1997, AJ, 113, 162
Calzetti, D., Armus, L., Bohlin, R. C., et al. 2000, ApJ, 533, 682
Calzetti, D., Kinney, A. L., & Storchi-Bergmann, T. 1994, ApJ, 429, 582
```

```
Cardelli, J. A., Clayton, G. C., & Mathis, J. S. 1989, ApJ, 345, 245
Coil, A. L., Aird, J., Reddy, N., et al. 2015, ApJ, 801, 35
De Barros, S., Reddy, N., & Shivaei, I. 2016, ApJ, 820, 96
Eldridge, J. J., Stanway, E. R., Xiao, L., et al. 2017, PASA, 34, e058
Fanelli, M. N., O'Connell, R. W., & Thuan, T. X. 1988, ApJ, 334, 665
Förster Schreiber, N. M., Genzel, R., Bouché, N., et al. 2009, ApJ, 706, 1364
Fudamoto, Y., Oesch, P. A., Faisst, A., et al. 2020, arXiv:2004.10760
Fudamoto, Y., Oesch, P. A., Schinnerer, E., et al. 2017, MNRAS, 472, 483
Gordon, K. D., Clayton, G. C., Misselt, K. A., Landolt, A. U., & Wolff, M. J.
   2003, ApJ, 594, 279
Grogin, N. A., Kocevski, D. D., Faber, S. M., et al. 2011, ApJS, 197, 35
Kashino, D., Silverman, J. D., Rodighiero, G., et al. 2013, ApJL, 777, L8
Koekemoer, A. M., Faber, S. M., Ferguson, H. C., et al. 2011, ApJS, 197, 36
Kreckel, K., Groves, B., Schinnerer, E., et al. 2013, ApJ, 771, 62
Kriek, M., Shapley, A. E., Reddy, N. A., et al. 2015, ApJS, 218, 15
Leitherer, C. 1990, ApJS, 73, 1
Leung, G. C. K., Coil, A. L., Aird, J., et al. 2019, ApJ, 886, 11
Markwardt, C. B. 2009, in ASP Conf. Ser. 411, Astronomical Data Analysis
   Software and Systems XVIII, ed. D. A. Bohlender, D. Durand, & P. Dowler
   (San Francisco, CA: ASP), 251
McKee, C. F., & Ostriker, E. C. 2007, ARA&A, 45, 565
McLean, I. S., Steidel, C. C., Epps, H. W., et al. 2012, Proc. SPIE, 8446,
   84460I
Pannella, M., Elbaz, D., Daddi, E., et al. 2015, ApJ, 807, 141
Papovich, C., Finkelstein, S. L., Ferguson, H. C., Lotz, J. M., & Giavalisco, M.
   2011, MNRAS, 412, 1123
Price, S. H., Kriek, M., Brammer, G. B., et al. 2014, ApJ, 788, 86
Reddy, N., Dickinson, M., Elbaz, D., et al. 2012a, ApJ, 744, 154
Reddy, N. A., Erb, D. K., Pettini, M., Steidel, C. C., & Shapley, A. E. 2010,
    ApJ, 712, 1070
Reddy, N. A., Kriek, M., Shapley, A. E., et al. 2015, ApJ, 806, 259
Reddy, N. A., Pettini, M., Steidel, C. C., et al. 2012b, ApJ, 754, 25
Reddy, N. A., Steidel, C. C., Erb, D. K., Shapley, A. E., & Pettini, M. 2006,
Reddy, N. A., Steidel, C. C., Pettini, M., & Bogosavljević, M. 2016, ApJ,
   828, 107
Shapley, A. E., Steidel, C. C., Pettini, M., & Adelberger, K. L. 2003, ApJ,
   588, 65
Shivaei, I., Reddy, N., Rieke, G., et al. 2020, ApJ, 899, 117
Skelton, R. E., Whitaker, K. E., Momcheva, I. G., et al. 2014, ApJS, 214, 24
Stanway, E. R., Eldridge, J. J., & Becker, G. D. 2016, MNRAS, 456, 485
Steidel, C. C., Rudie, G. C., Strom, A. L., et al. 2014, ApJ, 795, 165
Steidel, C. C., Strom, A. L., Pettini, M., et al. 2016, ApJ, 826, 159
Theios, R. L., Steidel, C. C., Strom, A. L., et al. 2019, ApJ, 871, 128
Topping, M. W., Shapley, A. E., Reddy, N. A., et al. 2020, MNRAS, 495, 4430
Wild, V., Charlot, S., Brinchmann, J., et al. 2011, MNRAS, 417, 1760
Wuyts, S., Förster Schreiber, N. M., Lutz, D., et al. 2011, ApJ, 738, 106
Wuyts, S., Förster Schreiber, N. M., Nelson, E. J., et al. 2013, ApJ, 779, 135
Yoshikawa, T., Akiyama, M., Kajisawa, M., et al. 2010, ApJ, 718, 112
```